

Probing a quantum spin liquid with equilibrium and nonequilibrium hole dynamics

J. H. Nyhegn,¹ K. Knakkegaard Nielsen,² and G. M. Bruun¹

¹*Center for Complex Quantum Systems, Department of Physics and Astronomy,
Aarhus University, Ny Munkegade, DK-8000 Aarhus C, Denmark*

²*Max-Planck Institute for Quantum Optics, Hans-Kopfermann-Str. 1, D-85748 Garching, Germany*

The properties and experimental identification of quantum spin liquids (QSLs) remain an important topic with many fundamental questions. Here, we explore the dynamics of a single charge dopant (hole) in a t - J_1 - J_2 model on a square lattice, which realizes a gapless \mathbb{Z}_2 QSL at half filling. Using a field theory approach based on the parton construction, which includes an infinite number of scatterings between the low-energy quasiparticle excitations of the QSL via a self-consistent Born approximation, we calculate both the equilibrium and nonequilibrium properties of the hole for weak and strong interactions. Quasiparticle branches as well as stringlike excitations of the holon are identified, and we furthermore explore the time-dependent spreading of a hole throughout the QSL after it has been injected at a given lattice site. The final ballistic expansion speed is shown to exhibit a nonmonotonic behavior as a quantum phase transition between an antiferromagnetic and the QSL phase is crossed, which is caused by a qualitative change in the fundamental kinematics of the interactions between the hole and the surrounding spins. Our results demonstrate how charge dopants can be used as a quantum probe for QSLs and are directly relevant to optical lattice experiments with single site resolution.

I. INTRODUCTION

The fundamental nature of quantum spin liquids (QSLs) continues to attract great interest since these phases were first identified more than fifty years ago [1]. Quantum spin liquid phases such as resonating valence bond states are typically described as a fluid of strongly correlated spin singlets. The liquid or resonating character of the ground state means that it consists of a macroscopically large superposition of configurations with spin singlets covering the lattice, which can give rise to exotic properties such as long-range quantum entanglement, quasiparticle excitations with nontrivial statistics, and spin-charge separation [2–6]. Thanks to sophisticated analytical and numerical methods, our understanding of QSLs keeps improving [7–12]. There is also great progress on the experimental side, where a spin liquid phase has recently been realized using the new powerful quantum simulation platform based on Rydberg atoms in optical tweezer arrays [13]. There are furthermore promising prospects of realising spin liquids in optical lattice experiments [14–18]. Finally, the number of strongly correlated two-dimensional (2D) materials is growing including atomically thin transition metal dichalcogenide bilayers, which realize highly tunable moiré lattice systems where spin liquids are predicted to emerge [19–21].

A feature of QSLs is that they elude local magnetic order down to zero temperature [2]. This invalidates standard approaches such as spin-wave theory in handling these strongly interacting phases. Except for the Kitaev spin liquid offering an exact solution [22], this means that numerical tools such as variational Monte Carlo (VMC) and matrix product states (MPSs) have played an important role in exploring QSLs [10, 12, 23–25]. Moreover, a smoking gun observation of a QSL remains a great challenge. Exact diagonalization and recent MPS studies sug-

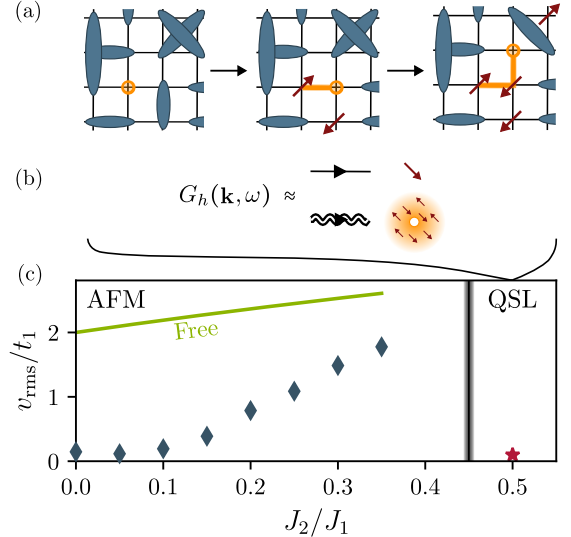


FIG. 1. (a) As a holon (orange circle) moves through a QSL, it distorts the spin singlets in its surroundings (blue ovals) leaving unpaired spins in its wake (arrows). These processes give rise to quasiparticle states as well as stringlike excitations of the holon. (b) The hole propagator is approximated by the uncorrelated copropagation of a dressed holon and a bare spinon. (c) The velocity of a hole spreading ballistically as a quasiparticle after being injected at a given lattice site. The expansion velocity increases with J_2/J_1 for $J_2/J_1 < 0.46$ (black vertical line) where the ground state is an AFM, but remains slower than a free particle (green line) with $v_{\text{rms}}/t_1 = 2\sqrt{1 + 2(t_2/t_1)^2}$, corresponding to a hole in a fully ferromagnetic background. For $J_2/J_1 > 0.46$, the ground state is a \mathbb{Z}_2 QSL and the expansion velocity is much smaller. This gives rise to a nonmonotonic behavior of the velocity with a maximum likely to be close to the quantum phase transition point $J_2/J_1 = 0.46$.

gest that the dynamical response from inserting charge dopants can be used as probes for these phases [26–28]. Understanding the dynamics of dopants in spin liquids is however challenging and has mostly been approached phenomenologically or at a mean-field level [5, 29–32]. In these studies, the focus has furthermore primarily been on the interactions with the gauge fluctuations.

These experimental advances make it timely to further explore the dynamics of a dopant in a QSL. In this paper, we focus on a hole in a so-called \mathbb{Z}_2 QSL realized in a t - J_1 - J_2 model at half filling. We develop a field theoretical approach for analyzing this, which is capable of describing the strong coupling regime by including an infinite number of scatterings between the hole and its surrounding spins via a self-consistent Born approximation (SCBA). Using this, we identify quasiparticles as well as stringlike excitations of the holon (See Fig. 1(a)). The resulting spectral function is shown to be quite different from that of a hole in an AFM, which indicates that it can be used to detect the presence of a QSL. We furthermore explore the nonequilibrium spreading of a hole throughout the lattice ensuing its injection at a specific lattice site. For long times, the hole is shown to expand ballistically as a quasiparticle whose speed depends non-monotonically on the ratio J_2/J_1 , with a maximum likely close to the quantum phase transition between the AFM and the QSL phases (See Fig. 1(c)). This nontrivial dependence provides another promising way to detect the QSL.

The paper is organized as follows. In Sec. II, we introduce the t - J_1 - J_2 model. We then discuss the parton construction and our field theoretical approach. The spectral properties of a holon are discussed in Sec. III. In Sec. IV, we explore the spectral properties of a physical hole as well as its nonequilibrium expansion dynamics. By comparing with the same properties of a hole in an AFM, we discuss in Sec. V two ways where the hole can be used as a quantum probe of a QSL. We end with conclusions and outlook in Sec. VI.

II. MODEL AND FIELD THEORY

We study the behavior of a single dopant in a \mathbb{Z}_2 QSL in the paradigmatic t - J model with both nearest (NN) and next-nearest neighbor (NNN) interactions

$$\hat{H} = \hat{H}_t + \hat{H}_J. \quad (1)$$

Here

$$\hat{H}_t = -t_1 \sum_{\langle i,j \rangle, \sigma} \tilde{c}_{i,\sigma}^\dagger \tilde{c}_{j,\sigma} - t_2 \sum_{\langle\langle i,j \rangle\rangle, \sigma} \tilde{c}_{i,\sigma}^\dagger \tilde{c}_{j,\sigma} + \text{H.c.} \quad (2)$$

is the hopping Hamiltonian with NN and NNN parameters t_1, t_2 , and

$$\hat{H}_J = J_1 \sum_{\langle i,j \rangle} \left[\hat{\mathbf{S}}_i \cdot \hat{\mathbf{S}}_j - \frac{1}{4} \hat{n}_i \hat{n}_j \right] + J_2 \sum_{\langle\langle i,j \rangle\rangle} \left[\hat{\mathbf{S}}_i \cdot \hat{\mathbf{S}}_i - \frac{1}{4} \hat{n}_i \hat{n}_j \right] \quad (3)$$

describes AFM Heisenberg type NN and NNN spin couplings $J_1, J_2 > 0$. The restricted fermionic operators $\tilde{c}_{i,\sigma}^\dagger = \hat{c}_{i,\sigma}^\dagger (1 - \hat{n}_i)$ ensure no double occupancy in terms of the on-site density operator $\hat{n}_i = \sum_\sigma \hat{c}_{i,\sigma}^\dagger \hat{c}_{i,\sigma}$. Here, $\hat{c}_{i,\sigma}$ removes a fermion with spin σ at site \mathbf{i} and $\hat{\mathbf{S}}_i = \frac{1}{2} \sum_{\sigma,\sigma'} \hat{c}_{i,\sigma}^\dagger \boldsymbol{\sigma}_{\sigma\sigma'} \hat{c}_{i,\sigma'}$. The spin coupling in Eq. (3) naturally arises as an effective low-energy description of superexchange processes in the Fermi-Hubbard model for large onsite repulsion U close to half filling, where $J_1 = 4t_1^2/U$ and $J_2 = 4t_2^2/U$. As this is relevant for strongly correlated 2D materials and experiments with atoms in optical lattices, we will in the following uphold these relations such that $J_2/J_1 = (t_2/t_1)^2$. To understand how the properties of the hole evolves with increasing interaction strength, we will, however, deviate from the limit $J_i/t_i \ll 1$.

At half filling, the Heisenberg model supports four distinct phases [33–36]. With no NNN interaction, the model exhibits antiferromagnetic (AFM) order. Turning on a nonzero J_2 , we initiate a competition that frustrates the magnetic order, and by increasing J_2/J_1 the system first enters a gapless \mathbb{Z}_2 QSL at $J_2/J_1 \sim 0.46$, then a valence bond solid (VBS) phase at $J_2/J_1 \sim 0.55$, and at last the magnetically ordered columnar phase at $J_2/J_1 \sim 0.6$. To explore the QSL phase, one, thus, needs to be able to achieve NNN hoppings $|t_2| \simeq |t_1|/\sqrt{2}$. While NNN hoppings in standard optical lattice experiments are inherently much smaller than the NN hoppings, optical superlattices have been shown [37] to allow the desired control over t_2/t_1 . Focusing on the QSL phase, we now turn to the parton construction.

A. Parton construction

Following Refs. [5, 38, 39], we decompose the fermions into partons as

$$\hat{c}_{i,\sigma} = \hat{b}_i^\dagger \hat{f}_{i,\sigma}, \quad (4)$$

where \hat{b}_i removes a bosonic holon at site \mathbf{i} describing the charge degree of freedom, and $\hat{f}_{i,\sigma}$ removes a fermionic spinon describing the spin degree of freedom. Using the parton decomposition in Eq. (3), the mean-field theory most accurately describing the ground state for $J_2 \simeq 0.5J_1$ at half filling with no holons is found to be a gapless \mathbb{Z}_2 spin liquid [10, 34, 36, 40, 41]. From VMC results, the optimal mean-field parton Hamiltonian was found to be

$$\hat{H}_J = \sum_{\mathbf{k},\sigma} \epsilon_{\mathbf{k}} \hat{f}_{\mathbf{k},\sigma}^\dagger \hat{f}_{\mathbf{k},\sigma} + \sum_{\mathbf{k}} \left(\Delta_{\mathbf{k}} \hat{f}_{\mathbf{k},\uparrow}^\dagger \hat{f}_{-\mathbf{k},\downarrow}^\dagger + \text{h.c.} \right), \quad (5)$$

with the BCS-type pairing functions [8, 10, 41]

$$\epsilon_{\mathbf{k}} = \epsilon(\cos k_x + \cos k_y) \\ \Delta_{\mathbf{k}} = \Delta_1(\cos k_x - \cos k_y) + \Delta_2 \sin(2k_x) \sin(2k_y), \quad (6)$$

where we have taken the lattice constant to unity. Within the theory of the projective-symmetry group, this spin

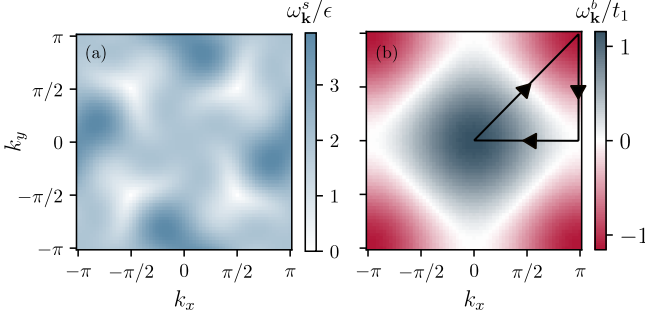


FIG. 2. (a) Spinon spectrum given by Eq. (8) with $\Delta_1 = 1.1\epsilon$ and $\Delta_2 = 1.8\epsilon$. (b) Bare holon spectrum given by Eq. (11).

liquid is denoted Z2Azz13 [8]. Instead of determining the parameters in Eq. (6) via their self-consistent mean-field relations to the Heisenberg parameters J_1 and J_2 [42], we use unless otherwise stated the values $\Delta_1 = 1.1\epsilon$ and $\Delta_2 = 1.8\epsilon$, found as the optimal parameters in the VMC study [41] for $J_2/J_1 = 1/2$. Note that Eq. (5) is defined in an enlarged Hilbert space where unphysical doubly occupied sites are allowed keeping only the average number of particles per site fixed at unity. These unphysical states can be projected out by using the Gutzwiller operator $\hat{\mathcal{P}} = \prod_i (\hat{n}_{i,\downarrow} - \hat{n}_{i,\uparrow})^2$ [10, 24, 36, 42]. It has however been shown that the mean-field description given by Eq. (5) without a subsequent Gutzwiller projection accurately captures the low-energy excitations of the spin liquid state of the Heisenberg Hamiltonian \hat{H}_J taking $\epsilon \simeq J_1/3$ [43]. Not having to perform a Gutzwiller projection dramatically simplifies the description, and we therefore use this mean-field approach in the following to describe the QSL. Diagonalizing Eq. (5) then yields

$$\hat{H}_J = \sum_{\mathbf{k},\sigma} \omega_{\mathbf{k}}^s \hat{\gamma}_{\mathbf{k},\sigma}^\dagger \hat{\gamma}_{\mathbf{k},\sigma}, \quad (7)$$

with the spinon spectrum

$$\omega_{\mathbf{k}}^s = \sqrt{\epsilon_{\mathbf{k}}^2 + \Delta_{\mathbf{k}}^2}, \quad (8)$$

shown in Fig. 2(a). The BCS-type ground state is defined by $\hat{\gamma}_{\mathbf{k},\sigma}|\text{GS}\rangle = 0$. Note that the Cooper pairs in this mean-field theory correspond to the spin singlets.

The hopping term \hat{H}_t comes into play when we add a single dopant to the system. Using the parton construction yields

$$\hat{H}_t = -t_1 \sum_{\langle i,j \rangle} \hat{b}_i \hat{f}_{i,\sigma}^\dagger \hat{f}_{j,\sigma} \hat{b}_j^\dagger - t_2 \sum_{\langle\langle i,j \rangle\rangle} \hat{b}_i \hat{f}_{i,\sigma}^\dagger \hat{f}_{j,\sigma} \hat{b}_j^\dagger, \quad (9)$$

where we have removed the projection operators since we only consider a single dopant and allow multiple spinons on a given site [5, 38, 44]. Expressing this in terms of the spinon operators $\hat{\gamma}_{\mathbf{k},\sigma}^\dagger$ diagonalizing \hat{H}_J giving Eq. (7),

we can write Eq. (9) as

$$\begin{aligned} \hat{H}_t = & \sum_{\mathbf{k}} \omega_{\mathbf{k}}^b \hat{b}_{\mathbf{k}}^\dagger \hat{b}_{\mathbf{k}} + \sum_{\mathbf{k},\mathbf{k}',\mathbf{q},\sigma} h_{\mathbf{k},\mathbf{k}',\mathbf{q}} \hat{b}_{\mathbf{k}-\mathbf{q}}^\dagger \hat{b}_{\mathbf{k}} \hat{\gamma}_{\mathbf{k}',\sigma}^\dagger \hat{\gamma}_{\mathbf{k}'-\mathbf{q},\sigma} \\ & + \sum_{\mathbf{k},\mathbf{k}',\mathbf{q}} g_{\mathbf{k},\mathbf{k}',\mathbf{q}} \left(\hat{b}_{\mathbf{k}-\mathbf{q}}^\dagger \hat{b}_{\mathbf{k}} \hat{\gamma}_{\mathbf{k}',\uparrow}^\dagger \hat{\gamma}_{-\mathbf{k}'+\mathbf{q},\downarrow} + \text{h.c.} \right). \end{aligned} \quad (10)$$

Here

$$\omega_{\mathbf{k}}^b = 2 \sum_{\mathbf{k}'} \Gamma_{\mathbf{k}+\mathbf{k}'} v_{\mathbf{k}'}^2 \quad (11)$$

is the dispersion of a bare holon shown in Fig. 2(b), and

$$\begin{aligned} g_{\mathbf{k},\mathbf{k}',\mathbf{q}} &= -[\Gamma_{\mathbf{k}-\mathbf{k}'} u_{\mathbf{k}'} v_{\mathbf{k}'-\mathbf{q}} + \Gamma_{\mathbf{k}+\mathbf{k}'-\mathbf{q}} v_{\mathbf{k}'} u_{\mathbf{k}'-\mathbf{q}}] \\ h_{\mathbf{k},\mathbf{k}',\mathbf{q}} &= \Gamma_{\mathbf{k}-\mathbf{k}'} u_{\mathbf{k}'} u_{\mathbf{k}'-\mathbf{q}} - \Gamma_{\mathbf{k}+\mathbf{k}'-\mathbf{q}} v_{\mathbf{k}'} v_{\mathbf{k}'-\mathbf{q}} \end{aligned} \quad (12)$$

are the vertex functions with

$$\begin{aligned} \Gamma_{\mathbf{k}} &= \frac{2}{N} (t_1 [\cos k_x + \cos k_y] \\ &+ t_2 [\cos(k_x + k_y) + \cos(k_y - k_x)]) \end{aligned} \quad (13)$$

coming from NN and NNN structure factors. The number of lattice sites is N , and the coherence factors are $u_{\mathbf{k}} = \sqrt{(1 + \epsilon_{\mathbf{k}}/\omega_{\mathbf{k}}^s)/2}$ and $v_{\mathbf{k}} = \text{sgn} \Delta_{\mathbf{k}} \sqrt{(1 - \epsilon_{\mathbf{k}}/\omega_{\mathbf{k}}^s)/2}$. There are two kinds of interaction vertices between the holon and the spinons in Eq. (10): $h_{\mathbf{k},\mathbf{k}',\mathbf{q}}$ describes the scattering of a holon on a spinon whereas $g_{\mathbf{k},\mathbf{k}',\mathbf{q}}$ describes the emission/absorption of two spinons by a holon.

With Eqs. (7) and (10), we have arrived at our final Hamiltonian describing a dopant in a \mathbb{Z}_2 QSL. Staying true to the Fermi-Hubbard relation $J_i = 4t_i^2/U$, we use $t_2/t_1 = -\sqrt{J_2/J_1} = -1/\sqrt{2}$ throughout corresponding to the case of a single hole doping ($t_2/t_1 = 1/\sqrt{2}$ for a doublon [45]). We also keep the ratio $\Delta_2/\Delta_1 = 1.8/1.1$ fixed and $\Delta_1 = 1.1\epsilon$ unless otherwise stated, which leaves ϵ/t_1 as a free parameter in our theory. Strong interaction with the holon creating many spinon excitations corresponds to $\epsilon/t_1 \ll 1$ whereas $\epsilon/t_1 \gg 1$ corresponds to weak interaction.

B. Quantum field theory

We will now describe our quantum field theory approach to describe the motion of the hole in the QSL. In the parton construction, a first natural step is to analyze the motion of the holon quasiparticle [29, 32] as described with the retarded holon Green's function

$$G(\mathbf{k}, \tau) = -i\theta(\tau) \langle \{ \hat{b}_{\mathbf{k}}(\tau), \hat{b}_{\mathbf{k}}^\dagger(0) \} \rangle, \quad (14)$$

where $\hat{A}(\tau) = \exp(i\hat{H}\tau) \hat{A} \exp(-i\hat{H}\tau)$ is the operator at time τ in the Heisenberg picture and $\{\hat{A}, \hat{B}\} = \hat{A}\hat{B} + \hat{B}\hat{A}$. In frequency/momentum space, a formal solution for the Green's function is

$$G(\mathbf{k}, \omega) = \frac{1}{\omega - \omega_{\mathbf{k}}^b - \Sigma(\mathbf{k}, \omega) + i0^+}, \quad (15)$$

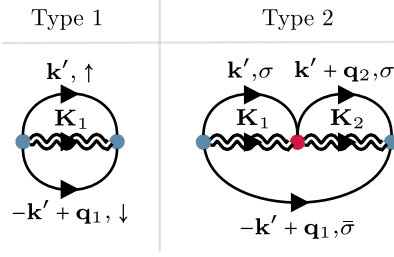


FIG. 3. Feynman diagrams included in the extended SCBA for the holon self-energy. Double wavy lines are the full holon propagator and the single lines are spinon propagators. The blue and red dots are the g and h vertices in Eq. (12) respectively.

where $\Sigma(\mathbf{k}, \omega)$ is the holon self-energy. In order to calculate the self-energy, one in general needs to resort to approximations. Here, we will apply the self-consistent Born approximation (SCBA) [44], which has proven to be very accurate for describing a mobile hole in an AFM even for strong interactions when compared to Monte Carlo calculations and exact diagonalization [46, 47]. Remarkably, this holds even for describing nonequilibrium hole dynamics [48]. In the present case with the two kinds of spinon-hole interaction vertices given by Eq. (12), the SCBA amounts to including the two types of diagrams for the holon self-energy shown in Fig. 3. These two diagrams give the exact solution of the self-energy to third order in the hopping amplitudes, and by using the self-consistent holon Green's function we include an infinite class of diagrams in order to describe the limit $\epsilon/t_1 \ll 1$ of strong interactions. The self-consistent diagrams in Fig. 3 give the self-energy

$$\begin{aligned} \Sigma(\mathbf{k}, \omega) = & \sum_{\mathbf{k}', \mathbf{q}_1} g_{\mathbf{k}, \mathbf{k}', \mathbf{q}_1}^2 G(\mathbf{K}_1, \omega - \omega_{\mathbf{k}'}^s - \omega_{-\mathbf{k}'+\mathbf{q}_1}^s) \\ & - 2 \sum_{\mathbf{q}_2} g_{\mathbf{k}, \mathbf{k}', \mathbf{q}_1} G(\mathbf{K}_1, \omega - \omega_{\mathbf{k}'}^s - \omega_{-\mathbf{k}'+\mathbf{q}_1}^s) h_{\mathbf{k}-\mathbf{q}_1, \mathbf{k}'+\mathbf{q}_2, \mathbf{q}_2} \\ & \times G(\mathbf{K}_2, \omega - \omega_{\mathbf{k}'+\mathbf{q}_2}^s - \omega_{-\mathbf{k}'+\mathbf{q}_1}^s) g_{\mathbf{k}, \mathbf{k}'+\mathbf{q}_2, \mathbf{q}_1+\mathbf{q}_2}, \end{aligned} \quad (16)$$

with $\mathbf{K}_n = \mathbf{k} - \mathbf{q}_1 - \dots - \mathbf{q}_n$. Thus, our field theoretical approach amounts to calculating the holon Green's function by solving Eqs. (15) and (16) self-consistently, which includes an infinite number of spinon excitations created by the holon.

III. HOLON PROPERTIES

We now describe the properties of a holon dynamics captured by its spectral function

$$A(\mathbf{k}, \omega) = -2\text{Im}[G(\mathbf{k}, \omega)], \quad (17)$$

which gives the energy spectrum of a holon injected with momentum \mathbf{k} into the spin liquid. As detailed in Appendix A, it turns out that the second diagram in Fig. 3

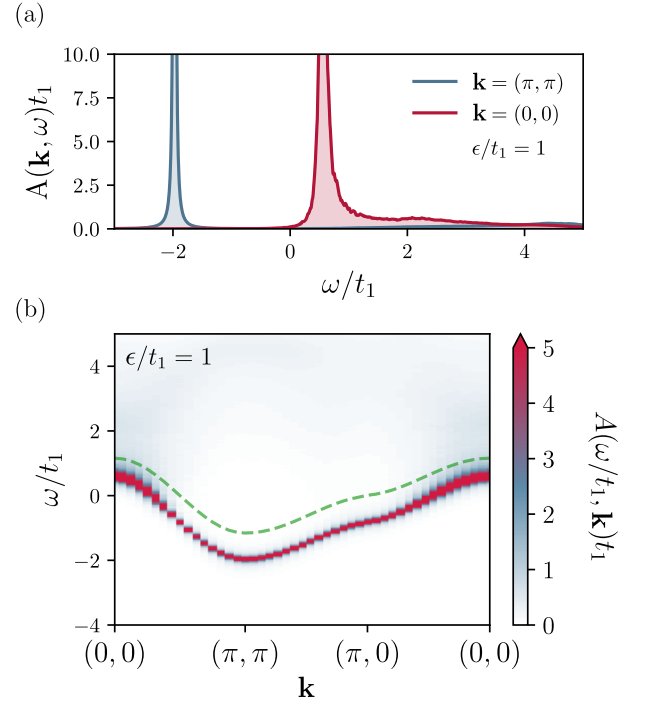


FIG. 4. (a) Spectral function of the holon for two different crystal momenta and the interaction strength $\epsilon/t_1 = 1$. (b) Spectral function for crystal momenta along the path in the Brillouin zone shown in Fig. 2(b). The green dashed line is the bare holon dispersion given by Eq. (11).

has only small effects on the self-energy and since it is computationally quite demanding to evaluate, it is omitted in the following.

Initiating the investigation in the weak coupling regime, we plot in Fig. 4(a) the holon spectral function for $\epsilon/t_1 = 1$ and two different momenta obtained by numerically solving Eqs. (15) and (16) self-consistently on a 32×32 lattice. We see that the spectral function exhibits a clear quasiparticle peak for both momenta. Figure 4(b) shows that the quasiparticle is well defined for all crystal momenta along the specified path in the Brillouin zone. The energy of this quasiparticle is due to interactions with the spinons shifted by a constant relative to the bare holon dispersion given by the green dashed line. We note that for all results, the spectral function obeys the sum rule $\int d\omega A_h(\mathbf{p}, \omega) = 2\pi$ with less than 1% deviation confirming the accuracy of our numerics.

Figure 5(a) shows that for intermediate interactions $\epsilon/t_1 = 0.5$, the quasiparticle peak in the holon spectral function has lost significant spectral weight to a many-body continuum. Indeed, the quasiparticle is completely washed out for momenta around $\mathbf{k} = (0, 0)$, which can be attributed to the emissions of spinon pairs as described by the first Feynman diagram in Fig. 3. The on-shell energies of these emissions form a continuum between $\min/\max\{\omega_{\mathbf{k}-\mathbf{q}}^b + \omega_{\mathbf{k}'}^s + \omega_{-\mathbf{k}'+\mathbf{q}}^s\}$, shown as orange dashed lines in Fig. 5(a). We clearly see that the quasiparticle is

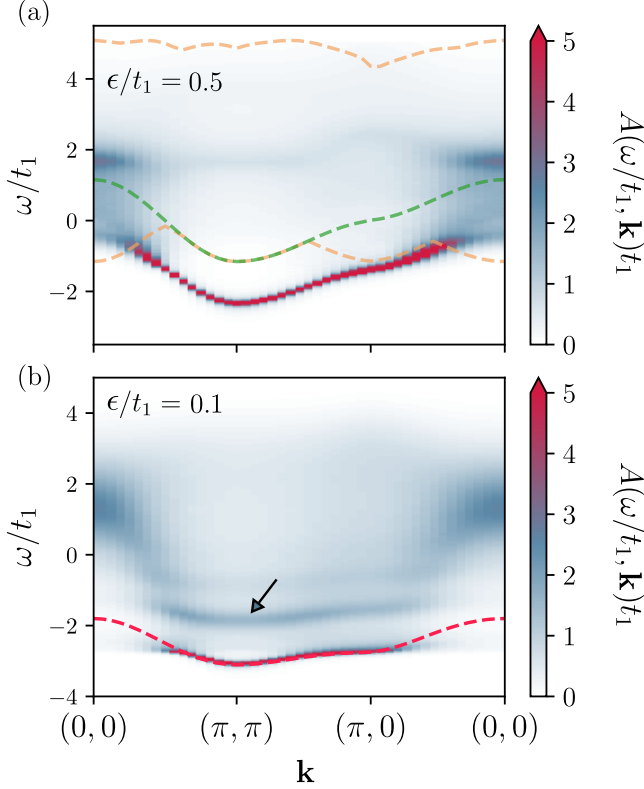


FIG. 5. Spectral function of the holon along the same path in the Brillouin zone as in Fig. 4, but now for intermediate interaction strength $\epsilon/t_1 = 0.5$ (a) and strong interaction strength $\epsilon/t_1 = 0.1$ (b). The dashed green line in (a) is again the bare holon dispersion given by Eq. (11) whereas the orange lines indicate the boundaries of the spinon-holon many-body continuum. The red dashed line in (b) is a fit to the holon dispersion; see Appendix E.

heavily damped when its energy is inside this continuum. Increasing the interacting strength further to $\epsilon/t_1 = 0.1$, Fig. 5(b) shows that the quasiparticle peak is damped even more due to decay into spinon modes as expected. We find that the width of the quasiparticle band is approximately given by $3.9\epsilon/t_1$; i.e., increasing the interaction strength decreases the bandwidth. This reflects that increasing the dressing of the holon by spinon modes results in a heavier quasiparticle. Such significant dressing cannot be captured by mean-field approaches, which in stark contrast predict a holon quasiparticle with a dispersion scaling as $\sim t_1$ [29, 49]. Our results are on the other hand consistent with MPS calculations for a chiral spin liquid predicting similar features for the physical hole [27]. We will analyze the properties of a physical hole in Sec. IV.

A. String excitations

Intriguingly, one can also see several additional bands at higher energies in Fig. 5(b). To investigate the origin of these bands, we plot in Fig. 6(a) the spectral function for momentum $\mathbf{p} = (\pi, \pi)$ as a function of ϵ/t_1 , clearly demonstrating that more excited states emerge with increasing interaction strength. Figure 6(b) gives strong evidence that the energy of these excited states scale as $(\epsilon/t_1)^{2/3}$. The ground state does not exhibit such a scaling coming from a continuum description, which could be due to its small spatial size making lattice effects important. For a hole in an AFM, such a scaling is interpreted as a smoking gun for the presence of so-called string excitations [50]. The basic mechanism is that the hole leaves a trace of frustrated spins in its wake as it moves through the AFM, which means that it experiences a linear potential. This gives rise to string states with the characteristic energy scaling in the continuum limit. Based on this, we conjecture that the bands in Fig. 5(b) also arise from string excitations of the holon. While there is no local magnetic order in a spin liquid, the holon still distorts its surroundings by creating pairs of spinon excitations as it moves through the lattice. This is explicitly evident in Eq. (10) and Fig. 3, and is illustrated in Fig. 1(a). The result is that the holon experiences a linear potential in real space leading to the excited string states visible in Fig. 5(b). The resonating valence bond (RVB) background can repair the frustration created by the holon. The time-scale of this is given by ϵ whereas the time scale of the hopping is given by t_i . The string states must therefore be expected to emerge when $\epsilon/t_i \ll 1$, which indeed is what we observe. To support this hypothesis further, we plot in Fig. 6(c) the energies of the excited states as a function of the spinon excitation energy averaged over the Brillouin zone $\omega_{avg}^s = \sum_{\mathbf{k}} \omega_{\mathbf{k}}^s / N$. The different colors correspond to calculations with different ratios of Δ_1/ϵ . Figure 6(c) shows that these different calculations collapse on a single line corresponding to the excitation energy scaling as $(\omega_{avg}^s/t_1)^{2/3}$. This confirms that the low-energy states can be understood as string excitations coming from the holon breaking spin singlets into individual spinons so that it experiences a linear potential with a strength $\propto \omega_{avg}^s$. In Appendix B, we further investigate the nature of these string excitations and find that they are suppressed if one increases the average length of the spin singlets.

IV. PROPERTIES OF PHYSICAL HOLES

We are now ready to explore the properties of the physical holes, which are the ones observable in experiments. To do this, we consider the hole Green's function

$$\begin{aligned} G_{h\sigma}(\mathbf{k}, \tau) &= -i\theta(\tau) \langle \{\hat{c}_{\mathbf{k},\sigma}(\tau), \hat{c}_{\mathbf{k},\sigma}^\dagger(0)\} \rangle \\ &= -i\theta(\tau) \langle \hat{c}_{\mathbf{k},\sigma}(\tau) \hat{c}_{\mathbf{k},\sigma}^\dagger(0) \rangle = \theta(\tau) G_h^>(\mathbf{k}, \tau). \end{aligned} \quad (18)$$

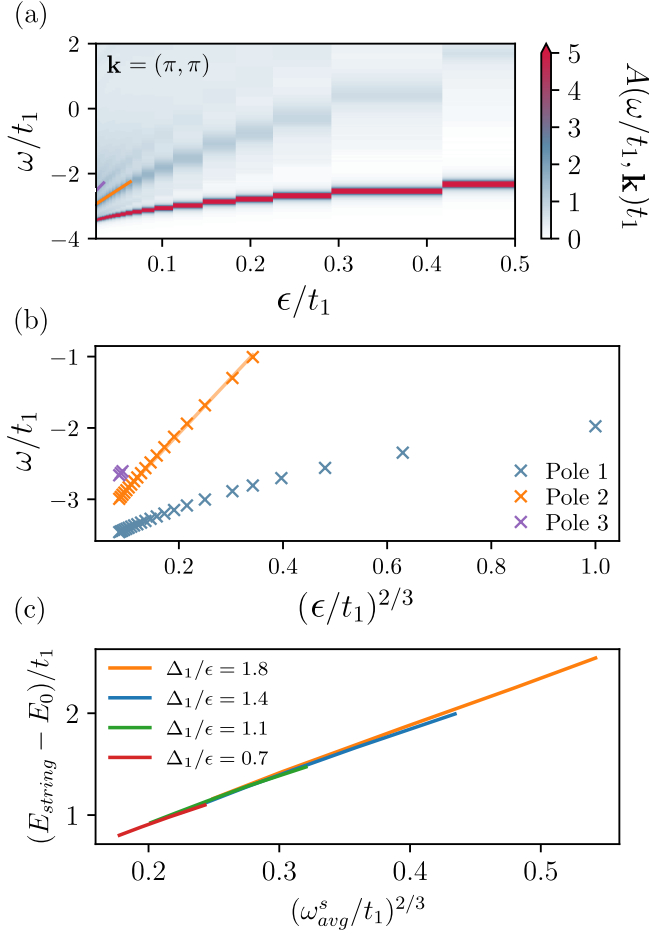


FIG. 6. (a) The holon spectral function for crystal momentum (π, π) as a function of the interaction strength ϵ/t_1 . (b) Energy of the three lowest bands in (a) replotted as a function of $(\epsilon/t_1)^{2/3}$. (c) Excitation energy $(E_{string} - E_0)/t_1$ of the lowest string band for momentum (π, π) as a function of $(\omega_{avg}^s/t_1)^{2/3}$. ω_{avg}^s is the average energy of a spinon, and E_0 is the energy of excitation at $\epsilon/t_1 = 0$

The second identity follows from the fact that only the single hole injected is present in the lattice, and it is crucial for enabling us to describe the nonequilibrium dynamics without having to use more cumbersome Keldysh techniques, as will be exploited in Sec. IV B.

Using the parton construction, the hole Green's function becomes a two-body Green's function

$$G_h(\mathbf{k}, \tau) = -\frac{i}{N} \sum_{\mathbf{q}_1, \mathbf{q}_2} \left\langle \hat{f}_{\mathbf{k}+\mathbf{q}_2, \sigma}^\dagger(\tau) \hat{b}_{\mathbf{q}_2}(\tau) \hat{b}_{\mathbf{q}_1}^\dagger \hat{f}_{\mathbf{k}+\mathbf{q}_1, \sigma} \right\rangle, \quad (19)$$

describing a spinon-holon "particle-hole" bubble. Here and in the following, we suppress the spin index on the Green's function since it does not depend on the direction of the spin due to the $SU(2)$ spin symmetry of the Fermi-Hubbard model. Writing it in terms of the rotated

spinons gives

$$G_h(\mathbf{k}, \tau) = \frac{-i}{N} \sum_{\mathbf{q}_1, \mathbf{q}_2} v_{\mathbf{k}+\mathbf{q}_1} v_{\mathbf{k}+\mathbf{q}_2} \left\langle \hat{\gamma}_{-\mathbf{k}-\mathbf{q}_2, \downarrow}(\tau) \hat{b}_{\mathbf{q}_2}(\tau) \hat{b}_{\mathbf{q}_1}^\dagger \hat{\gamma}_{-\mathbf{p}-\mathbf{q}_1, \downarrow}^\dagger \right\rangle. \quad (20)$$

Since $G_h(\mathbf{k}, \tau)$ is now transformed into a two-body Green's function due to the parton construction, it is in general very challenging to calculate. As depicted in Fig. 1(b), we resort to approximating it with the lowest-order diagram

$$G_h(\mathbf{k}, \omega) \approx \text{diagram} = \frac{1}{N} \sum_{\mathbf{q}} v_{\mathbf{k}+\mathbf{q}}^2 G(\mathbf{q}, \omega - \omega_{\mathbf{k}+\mathbf{q}}^s), \quad (21)$$

describing the uncorrelated motion of a bare spinon and a dressed holon. We find that this approximation obeys the frequency sum rule for the resulting hole spectral function within 1%. Equation (21) is in fact in the spirit of the parton construction, where a physical particle (hole) is expected to split into a spin and charge part. This assumption may however break down in certain (small) regions of the Brillouin zone, which is a fundamental and interesting question to be examined in future work.

A. Spectral properties

To explore the spectral properties of the physical hole, measurable with ARPES [27, 28], we plot in Fig. 7(a) its spectral function

$$A_h(\mathbf{k}, \omega) = -2\text{Im}[G_h(\mathbf{k}, \omega)] \quad (22)$$

calculated numerically from Eqs. (21) and (22) for the case of weak interactions $\epsilon/t_1 = 1$. We clearly see a quasiparticle-like band, which however is significantly broadened compared to the corresponding holon quasiparticle band in Fig. 4(b). It follows from Eq. (21) that the hole spectral function $A_h(\mathbf{k}, \omega)$ is nonzero for energies satisfying $\omega \approx \omega_{\mathbf{q}}^{\text{QP}} + \omega_{\mathbf{k}+\mathbf{q}}^s$. The dispersion of the hole band is in fact to a very good approximation given by

$$\omega_{\mathbf{k}}^h = \omega_{\mathbf{k}+\boldsymbol{\pi}}^{\text{QP}} + \omega_{\boldsymbol{\pi}}^s \quad (23)$$

with $\boldsymbol{\pi} = (\pi, \pi)$ as shown by the green dashed line in Fig. 7(a). This can be understood from the fact that the spinon spectrum shown in Fig. 2(a) has two Van Hove singularities at the center and corners of the Brillouin zone. While the coherence factor $v_{\mathbf{k}+\mathbf{q}}^2$ in Eq. (21) vanishes at the origin suppressing its contribution to the hole spectral function, the Van Hove singularity at $\boldsymbol{\pi}$ gives rise to a large contribution to the hole spectral function, which in turn gives a band with a dispersion given by Eq. (23). Similar features were reported in Ref. [28], where a hole in a Kitaev spin liquid was investigated using MPS methods.

In order to further explore how the spin environment affects the properties of the hole, we plot in Fig. 7(b) its

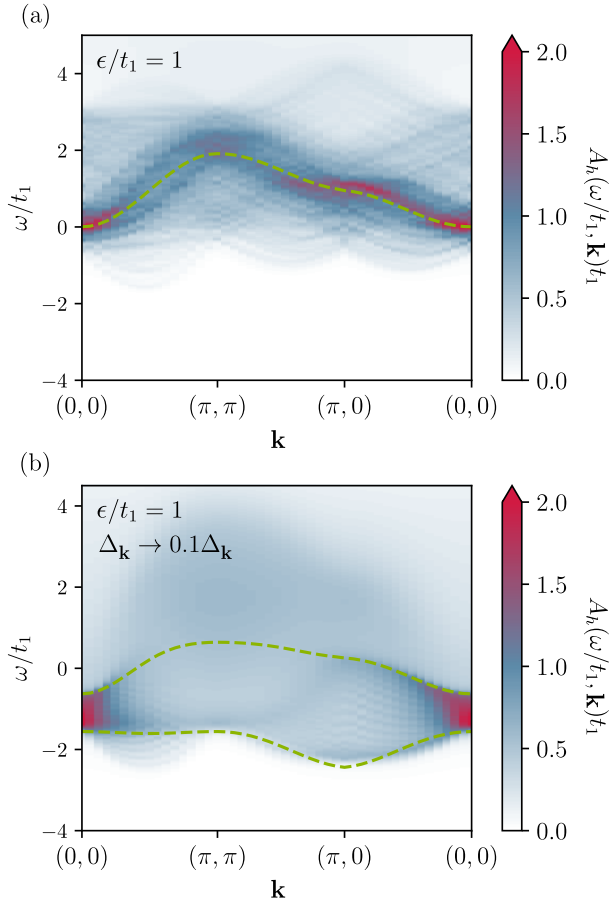


FIG. 7. (a) Spectral function of a physical hole along the same path in the Brillouin zone as in Fig. 4 for interaction strength $\epsilon/t_1 = 1$ and $\Delta_1 = 1.1\epsilon$. The green dashed line is Eq. (23). In panel (b) the pairing field is taken to be ten times smaller with the top green dashed line showing Eq. (23) and the bottom green dashed line $\omega = \omega_{\mathbf{k}+(0,\pi)}^{\text{QP}} + \omega_{(0,\pi)}^s$.

spectral function where we have used the same parameters as in Fig. 7(a) except for a smaller pairing potential $\Delta_{\mathbf{k}} \rightarrow 0.1\Delta_{\mathbf{k}}$. Since the length of the singlets is determined by the BCS coherence length $\propto 1/\Delta$, this makes them longer; see Appendix B. Figure 7(b) shows that the spectral function of the physical hole in turn becomes much broader with no clearly visible band except for small momenta, reflecting the increased dressing of the underlying holon by spinons. The many-body continuum of the hole spectral function is approximately bounded from below by the energy $\omega_{\mathbf{k}+(0,\pi)}^{\text{QP}} + \omega_{(0,\pi)}^s$, which comes from a new Van Hove singularity in the spinon spectrum at $\mathbf{k} = (0, \pi)$. These results show that the hole spectrum is broadened with less visible energy bands for spin liquids with longer singlets and a softer spinon spectrum.

In Sec. III A, we saw that the holon spectrum exhibits string excitations and we now investigate whether they are present also for the physical hole. Figure 8 shows the hole spectral function for strong interactions $\epsilon/t_1 = 0.1$

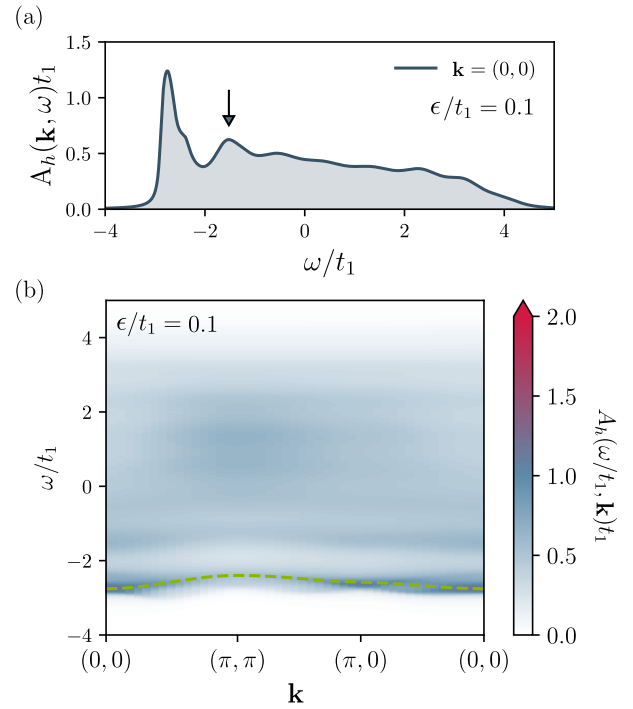


FIG. 8. (a) Spectral function of a physical hole for momentum $\mathbf{p} = \mathbf{0}$ and strong coupling $\epsilon/t_1 = 0.1$. The arrow indicates a string excitation. In (b), the spectral function is plotted along the same path in the Brillouin zone as in Fig. 4. The green dashed line shows Eq. (23).

again taking $\Delta_1/\epsilon = 1.8$ where the spectral function of the holon in Fig. 5(b) exhibits clear string excitation bands. While the spectrum as expected is quite broad, there is still a band visible with an energy given by Eq. (23) shown by the green dashed line. Importantly, we also see distinct bands at higher energies and as analyzed further in Appendix D, they are a direct consequence of the string excitations of the holon. Hence, we conclude the physical hole spectral response can exhibit sharp lines, which arise due to the string like excitations of the holon. Such lines have previously been interpreted as spinon-holon bound states [29, 30, 49].

B. Real space nonequilibrium dynamics

In a recent ground-breaking optical lattice experiment, the nonequilibrium motion of a hole after its release from a given lattice site in an AFM was explored in real space with single site resolution [51]. In light of this experiment and the prospects of realising spin liquids in optical lattices [14–18], we therefore now turn to investigating the real-space dynamics following a sudden insertion of a hole.

Concretely, we calculate the hole Green's function $G_h^>(\mathbf{r}, \tau) = -i\langle \hat{c}_{\mathbf{r},\sigma}(\tau) \hat{c}_{\mathbf{0},\sigma}^\dagger \rangle$ in real space and time, which

can be obtained from $G_h^>(\mathbf{k}, \omega)$ by Fourier transforming. As discussed below Eq. (18), this gives us access to the nonequilibrium dynamics described by the overlap of taking out a bare hole at site \mathbf{r} and time $\tau > 0$ after it was inserted at the origin at time $\tau = 0$. Note that in order to describe all dynamics, one needs the full time-dependent many-body wave function which is a much harder problem [48]. However, the bare hole dynamics described by $G_h^>(\mathbf{r}, \tau)$ is sufficient to explore the long-time dynamics as has been successfully exploited both for magnetic polarons in AFMs [48, 52] and for polarons in atomic gases [53, 54].

In Fig. 9(a), we show an example of such calculations. We plot the the overlap $|G_h^>|$ in real space for two different times after the hole has been injected at the origin at time $\tau = 0$ for the interaction strength $\epsilon/t_1 = 0.25$. This clearly shows how the hole spreads out through the lattice in a dynamical fashion. Note that the accumulated probability obtained by integrating the signal over the entire lattice is much larger in the left panel in Fig. 9(a) than in the right. This reflects that the hole becomes increasingly dressed with spinons as it moves through the lattice, so that the total probability of observing a *bare* hole decreases. The slight symmetry breaking barely visible in the lower panel is an artifact of the gauge choice in the mean-field description of the QSL.

In Fig. 9(b), we plot the gauge-invariant rms distance of the hole from its initial position at the origin defined as

$$d_{\text{rms}}(\tau) = \sqrt{\frac{\sum_{\mathbf{r}} r^2 |G_h^>(\mathbf{r}, \tau)|^2}{\sum_{\mathbf{r}} |G_h^>(\mathbf{r}, \tau)|^2}}. \quad (24)$$

The denominator takes care of the decreasing probability to observe a bare hole with time. Figure 9(b) shows that after some initial nontrivial dynamics, the hole expands ballistically with a speed that decreases with increasing interaction strength. Physically, the reason is that the hole becomes increasingly dressed by spinons making it heavier. Indeed, similar results were found regarding the expansion of a hole in an AFM both theoretically [48, 52, 55] and experimentally [51].

Figure 9(c) plots the final velocity, $v_{\text{rms}} = \partial_{\tau} d_{\text{rms}}$, of this ballistic expansion as a function of the interaction strength, which clearly shows this decrease. We also plot in Fig. 9(c) the bandwidth of the lowest band of the hole spectral function obtained from plots like those in Sec. IV A. The agreement between these two quantities in Fig. 9(c) demonstrates that for long times, the hole expands as a quasiparticle with a dispersion determined by the lowest band in its spectral function. As this band becomes flatter with increasing interaction strength reflecting to dressing of the bare holon with spinons, it slows down.

Again, deviating from the optimal VMC parameters by decreasing Δ_1/ϵ while keeping Δ_1/Δ_2 constant, we see in Fig. 9(d) that a spin environment with longer singlets slows down the expansion of the hole. This is

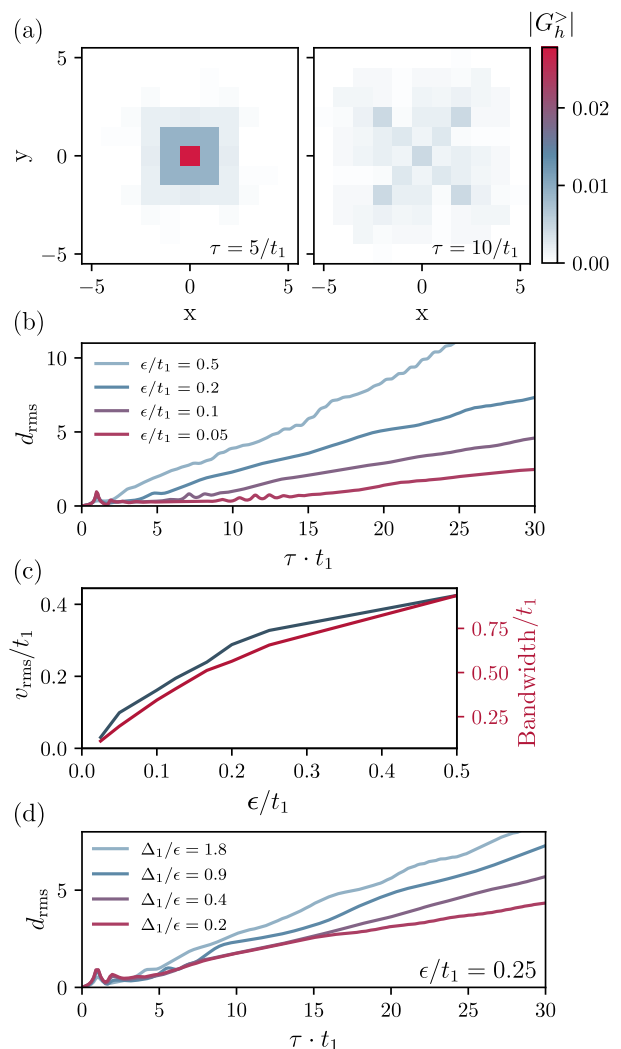


FIG. 9. (a) The expansion of the hole throughout the lattice at times $\tau = 5/t_1$ (left) and $\tau = 10/t_1$ (right) after it was injected at the origin, as parametrized by $|G_h^>|$. The interaction strength is $\epsilon/t_1 = 0.25$. (b) The rms distance from its initial position of an expanding hole defined by Eq. (24) as a function of time for different interaction strengths. (c) The associated long-time expansion speed as a function of interaction strength (blue line). The red line gives the bandwidth of the lowest hole quasiparticle band. (d) The rms distance as a function of time for the interaction strength $\epsilon/t_1 = 0.25$ and different pairing strengths Δ_1/ϵ with Δ_1/Δ_2 constant.

due to longer singlets leading to more low-lying spinon excitations, which increase the dressing of the holon. It illustrates how the expansion of the hole can probe the spin environment in a QSL phase.

V. THE HOLE AS A QUANTUM PROBE

A central problem regarding QSLs is how to detect them. Armed with our field theoretical formalism ca-

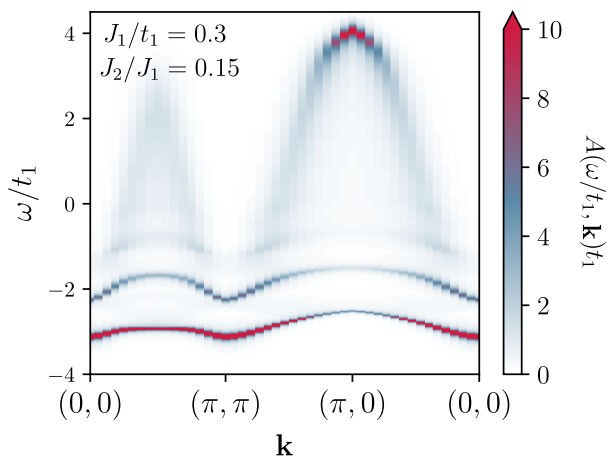


FIG. 10. Spectral function of a hole along the same path in the Brillouin zone as in Fig. 4 for $J_1/t_1 = 0.3$, $J_2/J_1 = 0.15$, and $t_2/t_1 = -\sqrt{J_2/J_1}$, where the system is in an AFM phase.

pable of describing both equilibrium and nonequilibrium dynamics, we will in this section suggest two ways to use a hole as a quantum probe for spin liquids.

In order to do this, we compare the spectral as well as expansion properties of a hole in a QSL with those in an AFM, which is the ground state of the Heisenberg model \hat{H}_J for small J_2 [33, 34, 40]. To calculate the properties of a hole in an AFM, we use linear spin wave theory combined with the SCBA, which has been shown to be remarkably accurate both for the equilibrium and nonequilibrium properties [44, 46–48, 52, 56–62]. We refer the reader to Refs. [48, 52, 61, 62] and Appendix C for the technical details of this method.

Let us first compare the spectral properties of a hole in an AFM and in a QSL. In Fig. 10, we show the spectral function of the hole in an AFM for $J_2/J_1 = 0.15$, $t_2/t_1 = -\sqrt{J_2/J_1}$, and $J_1/t_1 = 0.3$. Using $J_1 \simeq 3\epsilon$ for the QSL [43], the latter ratio corresponds to $\epsilon/t_1 \sim 0.1$. It is therefore natural to compare Fig. 10 with Fig. 8(b), which shows the spectral function of a hole in a QSL with $\epsilon/t_1 = 0.1$ and $J_2/J_1 = 1/2$. We see that these two spectral functions are qualitatively different. Whereas the spectral function in the AFM phase has several sharp quasi-particle bands corresponding to a ground state quasi-particle and string excitations, which take up significant spectral weight, the spectral function in the QSL phase has significantly broader bands with a many-body continuum taking up much more weight. From this we conclude that the spectral function of a hole provides a promising way to detect a spin liquid. Similar results were reported in Ref. [27], where the spectral function for a hole in a chiral spin liquid was calculated using MPS methods.

Next, we compare the expansion dynamics of a hole in an AFM with that in a spin liquid, which can be measured in cold atom experiments. Our main result is shown in Fig. 1, which plots the long-time ballistic

expansion speed v_{rms} as a function of the ratio J_2/J_1 , where we have assumed that the spins form an AFM for $J_2/J_1 < 0.46$ indicated by the vertical black line, and a spin liquid for $J_2/J_1 > 0.46$ [33–35, 40, 41]. We see that the expansion speed of the hole increases with J_2/J_1 in the AFM phase. This may seem surprising at first since increasing J_2/J_1 leads to a softer spin-wave spectrum due to increased magnetic frustration, from which it would be tempting to conclude that the hole becomes more dressed and therefore slower in analogy with what happens in the QSL. The reason this does not occur is that a nonzero value of $t_2 = -\sqrt{J_2/J_1}t_1$ means that the hole can hop to the next-nearest neighbors without distorting the AFM background. This gives rise to a bare hole dispersion, which starts to dominate the dynamics as the AFM order decreases with J_2/J_1 eventually leading to an increase in ballistic expansion of a bare hole. At a fundamental level, the hole interacts with the AFM background by emitting or absorbing a *single* spin wave [44], and these scattering processes become off-resonant when the characteristic energy of the bare hole dispersion is much larger than the spin wave energies, from which it follows that hole becomes less dressed. This is also indicated by the fact that the hole initially experiences a slight slowdown for increasing J_2/J_1 . However, when the energy bandwidth of the bare hole exceeds the bandwidth of the spinwave spectrum, the dressing becomes inefficient and the hole speeds up.

The situation is qualitatively different in the QSL. Here, a basic interaction vertex corresponds to the emission or absorption of *two* spinons as can be seen in Eq. (10) and Fig. (3). This makes resonant spinon-holon scattering possible even when the characteristic energy of the spinon spectrum is much smaller than that of the bare holon. It follows that the holon and therefore the hole is always heavily dressed by spinons for strong interactions, even when the characteristic energy of the bare holon dispersion is large, which slows it down. While we unfortunately cannot calculate the hole velocity for more values of J_2/J_1 inside the QSL, since we are only aware of numerical results providing a mapping to the mean-field description for $J_2/J_1 = 1/2$ [41], our results do allow us to predict that the ballistic expansion velocity of a hole depends *nonmonotonically* on the ratio J_2/J_1 : In the AFM phase it increases whereas it becomes smaller again in the spin liquid phases as can be seen in Fig. 1. The maximum velocity of the hole is likely to occur close to the quantum phase transition between the AFM and the QSL, and since this result is due to the different kinematics in the hole-medium scattering in the two phases, we believe it is robust and not an artifact of any approximations. Hence, we conclude that observing the expansion dynamics of a hole is a promising way to detect the transition between an AFM and a QSL.

VI. CONCLUSIONS AND OUTLOOK

Inspired by the remarkable advances with experimental platforms based on optical lattices and 2D quantum materials, we explored the equilibrium and nonequilibrium properties of a hole in a QSL. Using a field theory approach, we identified the presence of quasiparticle stringlike states of the hole, originating from breaking up singlets into their constituent spinons. The hole was furthermore shown to expand ballistically as a quasiparticle throughout the QSL for long times after its injection at a given lattice site, with a velocity exhibiting a characteristic nonmonotonic behavior as a quantum phase transition between the AFM and the QSL phases is crossed. As such, our results suggests promising new ways to use the hole as a quantum probe for QSLs.

In addition to being relevant for new experiments exploring atoms in optical lattices and 2D quantum materials, our paper opens up several new research directions. This includes examining the possible presence of spinon-holon bound states, which in our field theory approach should show up as poles in the spinon-holon scattering matrix. It would be interesting to connect such calculations with earlier results stating that bound spinon-holon states are caused by an attractive interaction mediated by gauge fluctuations [5]. Another intriguing problem concerns the role of gauge fluctuations on the hole properties. While such gauge fluctuations likely are not important for the present \mathbb{Z}_2 QSL where they are gapped [8] and the low-energy spectrum of the mean-field description is similar to that after projection [43], it would be interesting to compare with calculations performed using VMC [63] and MPS methods [27, 28]. Gauge fluctuations are moreover crucial for describing other QSLs such as those realized in triangular lattices [8]. Finally, it would be very interesting to explore the binding of two holes in a QSL, which could lead to new and exotic superconductors/superfluids for a nonzero hole concentration.

ACKNOWLEDGMENTS

This work has been supported by the Danish National Research Foundation through the Center of Excellence “CCQ” (Grant Agreement No. DNR156), as well as by the Carlsberg Foundation through a Carlsberg Internationalisation Fellowship, Grant No. CF21.0410. J.H.N. would like to thank Leon Balents and Federico Becca for useful comments and discussions.

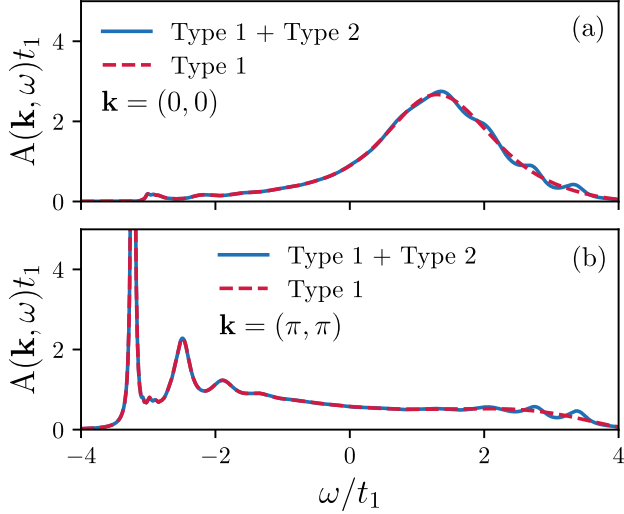


FIG. 11. Spectral function of the holon calculated using both types of diagrams from Fig. 3 (full line) and only type 1 (dashed line). These calculations are performed with $\epsilon/t_1 = 1/20$ for $\mathbf{k} = (\pi, \pi)$ in panel (a), $\mathbf{k} = (0, 0)$ in panel (b), and a lattice size of 8×8 . Except for small discrepancies at the top of the spectrum, we find that the overall behavior does not change by including the type 2 diagrams. This demonstrates the general tendency.

Appendix A: Extended self-consistent Born approximation

In this appendix, we investigate what happens if we include the type 2 diagrams from Fig. 3 when we calculate the Green's function of the holon, Eq. (15). Looking at types 1 and 2, we see that type 2 is a higher order diagram, with the order referring to the number of vertices. When including these diagrams, we, therefore, ensure that we keep the same order of diagrams. We do this by first including both types of diagrams in the iterative calculations, and then after 2/3 of the iterations we only include type 1. By including the type 2 diagrams, we cannot go much beyond a lattice size of 8×8 , but in Fig. 11 we see that including both types compared to only type 1 does not change the overall behavior of the spectral function. These two results represent the general tendencies. For the calculation in the main text we hence only include the type 1 diagrams in order to perform the calculations for larger system sizes.

Appendix B: String excitations

In this appendix, we further investigate the nature of the string excitations. We do this by tuning the pairing potentials Δ_1/ϵ while keeping Δ_1/Δ_2 constant. In doing this the average excitation energy of the spinons, ω_{avg}^s decreases, and we retrieve a softer spinon spectrum. This

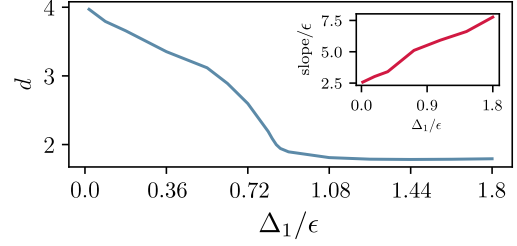


FIG. 12. Cooper pair length, Eq. (B1), for changing pairing potentials. As $\Delta_{\mathbf{k}}/\epsilon$ is increased, the average length of the Cooper pairs is lowered and flattens out around $\Delta_1/\epsilon = 1$. In the inset, we find the strength of string potential plotted as a function of Δ_1/ϵ .

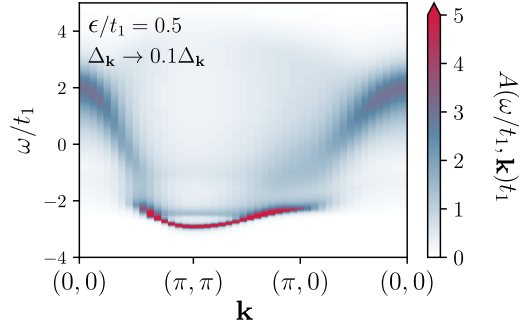


FIG. 13. Holon spectral function with $\epsilon/t_1 = 0.5$, $t_2/t_1 = -\sqrt{0.5}$, and $\Delta_{\mathbf{k}} \rightarrow 0.1\Delta_{\mathbf{k}}$ for a system size of 32×32 . Comparing with Fig. 5 we see that the QP bandwidth has decreased with a factor of 3 and that fewer crystal momenta state has a well defined peak.

results in a background with longer Cooper pairs and hence longer singlets, which is seen in Fig. 12 by plotting the average length of the Cooper pairs,

$$d = \sqrt{\frac{\sum_{\mathbf{d}} |\Delta_{\mathbf{d}}|^2 |\mathbf{d}|^2}{\sum_{\mathbf{d}} |\Delta_{\mathbf{d}}|^2}}, \quad \Delta_{\mathbf{d}} = \frac{1}{N} \sum_{\mathbf{r}} \langle \hat{f}_{\mathbf{r},\uparrow} \hat{f}_{\mathbf{r}+\mathbf{d},\downarrow} \rangle, \quad (\text{B1})$$

as a function of Δ_1/ϵ . In an environment with more low-lying excitations, we also find a much heavier quasi-particle; see Fig. 13. With the average cost of exciting the spinons decreasing, we would then expect the linear potential, given by the slope in Fig. 6, to decrease. This slope is plotted in the inset in Fig. 12, and we see just that. Another feature found is that, by decreasing the pairing potential, we need a larger interaction strength before the string excitations start to appear. In Fig. 14 we show results for $\Delta_{\mathbf{k}} \rightarrow 0.1\Delta_{\mathbf{k}}$ similar to those presented in Fig. 6(b). Here, we see that the first excited states at an interaction strength below $\epsilon/t_1 \sim 1/16$, and the ones corresponding to the third pole in Fig. 6(a) do not show for the ϵ/t_1 values shown. This behavior is summarized in Fig. 14(b), indicating for which parameters string excitations occur. This, therefore, means that

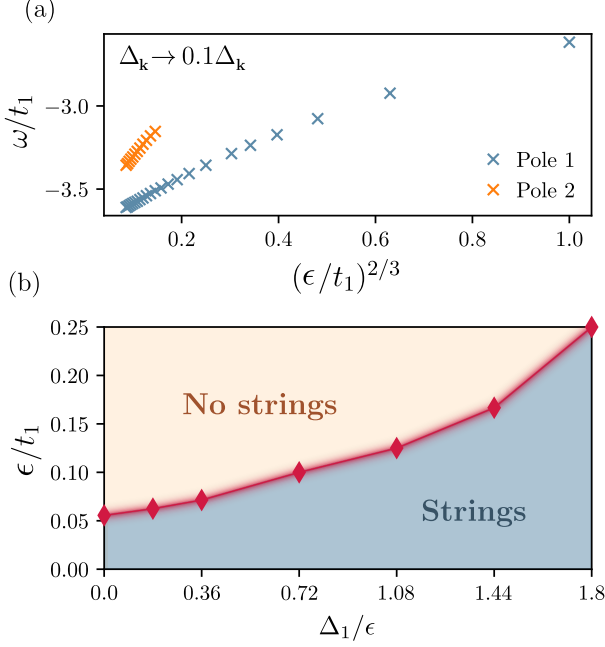


FIG. 14. Illustrating the importance of the pairing potential, we plot in panel (a) the poles of the Green's function as a function of the interaction strength with $\Delta_{\mathbf{k}} \rightarrow 0.1\Delta_{\mathbf{k}}$. The excited states do not show before $\epsilon/t_1 \sim 1/16$ which is at a three times larger interaction strength compared to the results presented in Fig. 6(b). Panel (b) summarizes the behavior by showing the interaction strength needed for the string excitations to show when the pairing potentials are changed. The red line illustrates when the string excitations show, and is the boundary between the blue region where no string excitations are present and the beige-colored region with string excitations present.

the tightly bound Cooper pairs promote the formation of these states. We believe the reason for this is the much heavier holon quasiparticle which hinders the formation of the strings.

Appendix C: Linear spin wave theory

In this appendix, we will use the linear spin wave theory (LSWT) on the t - J_1 - J_2 given by Eq. (2) and (3). Considering a single dopant, we will proceed as done previously [44, 46, 48, 52, 56, 57, 61, 62], utilizing a generalized Holstein-Primakoff. This relies on the system supporting AFM order, such that we can define two sublattices where the spins predominantly point up on sublattice A and down on sublattice B. Using this, we express the operators on sublattice A as $\hat{S}_{l,i}^z = (1 - \hat{h}_{l,i}^\dagger \hat{h}_{l,i})/2 - \hat{s}_{l,i}^\dagger \hat{s}_{l,i}$ and $\hat{S}_{l,i}^- = \hat{S}_{l,i}^x - i\hat{S}_{l,i}^y = \hat{s}_{l,i}^\dagger (1 - \hat{s}_{l,i}^\dagger \hat{s}_{l,i} - \hat{h}_{l,i}^\dagger \hat{h}_{l,i})^{1/2}$, and the creation operators are $\tilde{c}_{l,i,\downarrow} = \hat{h}_{l,i}^\dagger \hat{s}_{l,i}$ and $\tilde{c}_{l,i,\uparrow} = \hat{h}_{l,i}^\dagger (1 - \hat{s}_{l,i}^\dagger \hat{s}_{l,i} - \hat{h}_{l,i}^\dagger \hat{h}_{l,i})^{1/2}$. Opposite to the slave-boson description used in the main

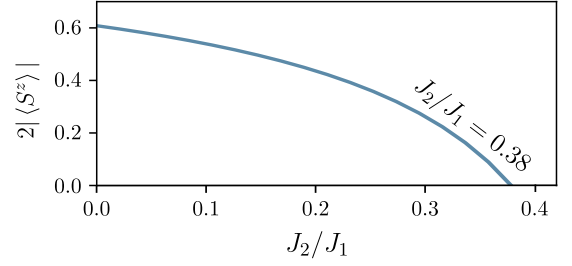


FIG. 15. The average magnetization, $2|\langle S_z \rangle| = 1 - 2 \sum_{\mathbf{k}} v_{\mathbf{k}}^2/N$, calculated within LSWT. This predicts a phase transition to occur at $J_2/J_1 = 0.38$.

text, $\hat{h}_{l,i}^\dagger$ is a fermionic creation operator of a hole, and $\hat{s}_{l,i}^\dagger$ is a bosonic creation operator describing derivation from the AFM ordered state. Similar relations are used for sublattice B.

Using these expressions and keeping only linear terms, we can diagonalize the J part of the Hamiltonian to find

$$\hat{H}_J = \sum_{\mathbf{k}} \omega_{\mathbf{k}}^m \hat{b}_{\mathbf{k}}^\dagger \hat{b}_{\mathbf{k}} + E_0, \quad (\text{C1})$$

with

$$\omega_{\mathbf{k}}^m = \frac{1}{2} \sqrt{\tilde{J}^2 - (\alpha_1 J_1 z \gamma_{\mathbf{k}})^2}, \quad \tilde{J}_{\mathbf{k}} \equiv z (J_1 + J_2 [\alpha_2 \gamma'_{\mathbf{k}} - 1]), \quad (\text{C2})$$

for $z = 4$ and $\gamma_{\mathbf{k}} = \sum_{\delta} e^{i\mathbf{k}\cdot\delta}/z$ and $\gamma'_{\mathbf{k}} = \sum_{\delta'} e^{i\mathbf{k}\cdot\delta'}/z$ being the structure factors for NN and NNN terms, respectively. The spin wave operators, \hat{b} , are related to the spin fluctuations, \hat{s} , by a Bogoliubov transformation

$$\begin{bmatrix} \hat{s}_{\mathbf{k}} \\ \hat{s}_{-\mathbf{k}}^\dagger \end{bmatrix} = \begin{bmatrix} u_{\mathbf{k}} & -v_{\mathbf{k}} \\ -v_{\mathbf{k}} & u_{\mathbf{k}} \end{bmatrix} \begin{bmatrix} \hat{b}_{\mathbf{k}} \\ \hat{b}_{-\mathbf{k}}^\dagger \end{bmatrix}, \quad (\text{C3})$$

where $u_{\mathbf{k}} = \sqrt{\frac{1}{2}(\tilde{J}/(2\omega_{\mathbf{k}}^m) + 1)}$ and $v_{\mathbf{k}} = \text{sgn}[\gamma_{\mathbf{k}}] \sqrt{\frac{1}{2}(\tilde{J}/(2\omega_{\mathbf{k}}^m) - 1)}$ are the coherence factors. Looking at Fig. 15, we see that this approach qualitatively captures the behavior when J_2 is increased. This predicts a phase transition to occur at $J_2/J_1 = 0.38$, which is not far from the predictions made with more advanced methods. This yields it to being around $J_2/J_1 \sim 0.46$ [33–36].

With the described transformations, the kinetic term takes the form

$$\hat{H}_t = \sum_{\mathbf{k}} \omega_{\mathbf{k}}^p \hat{h}_{\mathbf{k}}^\dagger \hat{h}_{\mathbf{k}} + \sum_{\mathbf{k}, \mathbf{p}} g(\mathbf{p}, \mathbf{k}) \hat{h}_{\mathbf{p}+\mathbf{k}}^\dagger \hat{h}_{\mathbf{p}} (\hat{b}_{-\mathbf{k}}^\dagger + \hat{b}_{\mathbf{k}}) \quad (\text{C4})$$

with

$$g(\mathbf{p}, \mathbf{k}) = \frac{zt_1}{\sqrt{N}} [u_{\mathbf{k}} \gamma_{\mathbf{p}+\mathbf{k}} - v_{\mathbf{k}} \gamma_{\mathbf{p}}], \quad (\text{C5})$$

and

$$\omega_{\mathbf{k}}^p = 2t_2 [\cos(k_x + k_y) + \cos(k_x - k_y)]. \quad (\text{C6})$$

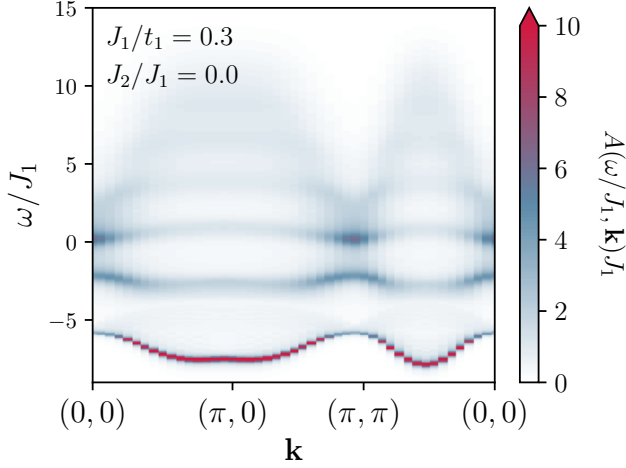


FIG. 16. Spectral function of a hole along the reversed path in the Brillouin zone as in Fig. 4 for $J_1/t_1 = 0.3$, $J_2/J_1 = 0$.

For a finite J_2 we hence get a bare dispersion corresponding to the hole jumping within the same sublattice. Proceeding as done in the literature [44, 46, 48, 52, 56, 57, 61, 62], we can use the above expressions to calculate the Green's function,

$$G(\mathbf{k}, \tau) = -i \langle T_\tau [\hat{h}_{\mathbf{k}}(\tau) \hat{h}_{\mathbf{k}}^\dagger(0)] \rangle, \quad (\text{C7})$$

of a single hole with the SCBA approximation. The spectral function of such result is presented in Fig. 16 for $J_2/J_1 = 0$ and $J_1/t_1 = 0.3$, which shows good agreement with the MPS result presented in Ref. [64].

Investigating the nature of the rms speedup as we approach the phase transition, we find that by neglecting the bare dispersion of the hole we retrieve an rms velocity which decreases with interaction strength; see Fig. 17. This we ascribe to the fact that with an increasing J_2/J_1 the spinon spectrum gets increasingly softer around $\mathbf{p} = (\pi, 0)$ and $\mathbf{p} = (0, \pi)$.

Appendix D: String excitations for hole

In this appendix, we show that indeed the higher excitation peaks in the hole's spectral function have the characteristic two-thirds scaling associated with string excitations. This is seen in Fig. 18, where we plot the energy of the peak as a function of $(\epsilon/t_1)^{2/3}$. Here, we see the linear behavior and in addition, we see that the energy is given by the energy of the holon string peak plus $\omega_{(\pi, \pi)}$ corresponding to the Van Hove singularity discussed in the main part. This shows that the excitation peaks in the hole spectral function come from the string excitations of the holon.

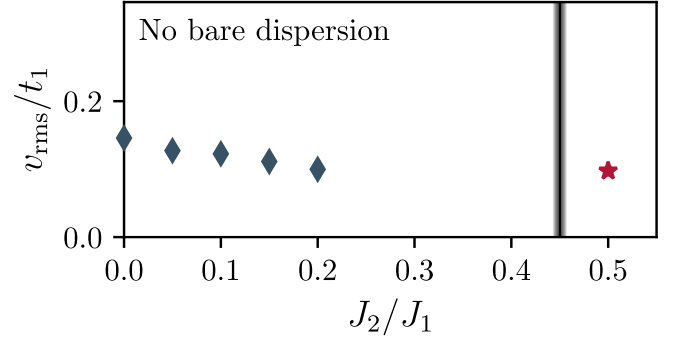


FIG. 17. Same plot as in Fig. 1, but where we have omitted the bare dispersion of the hole in the AFM phase. As we approach the phase transition from the AFM side, the hole experiences a slowdown instead of a speedup as in Fig. 1.

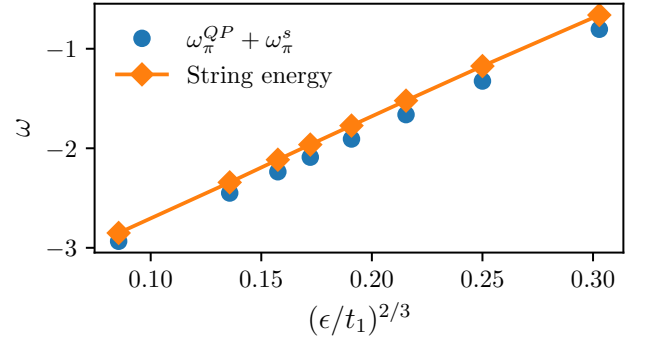


FIG. 18. Excitation energy of the excitation peak from the hole spectral function for $\mathbf{p} = (0, 0)$ in orange. Equivalent to Eq. (23), the blue data points show the energy of the holon excitation peak for $\mathbf{p} = (\pi, \pi)$ added to $\omega_{(\pi, \pi)}$ coming from the Van Hove singularity discussed in the main part. This is plotted as a function of $(\epsilon/t_1)^{2/3}$.

Appendix E: Quasiparticle band fit

Interestingly, we find that the lowest quasiparticle band can be fitted to the form

$$\omega_{\mathbf{k}}^{\text{QP}} = \tilde{t}_1(\cos k_x + \cos k_y) + \tilde{t}_2[\cos(k_x + k_y) + \cos(k_x - k_y)] + \tilde{t}_3(\cos 2k_x + \cos 2k_y), \quad (\text{E1})$$

shown as the red dashed line in Fig. 5(b), where $\tilde{t}_2/\tilde{t}_1 \approx 0.15$ and $\tilde{t}_3/\tilde{t}_1 \approx -0.05$. We find that these ratios are approximately constant for strong interaction strengths $\epsilon/t_1 < 0.1$.

-
- [1] P. Anderson, Resonating valence bonds: A new kind of insulator?, *Materials Research Bulletin* **8**, 153 (1973).
- [2] L. Savary and L. Balents, Quantum spin liquids: A review, *Reports on Progress in Physics* **80**, 016502 (2017).
- [3] C. Broholm, R. J. Cava, S. A. Kivelson, D. G. Nocera, M. R. Norman, and T. Senthil, Quantum spin liquids, *Science* **367**, eaay0668 (2020).
- [4] V. Kalmeyer and R. B. Laughlin, Equivalence of the resonating-valence-bond and fractional quantum Hall states, *Physical Review Letters* **59**, 2095 (1987).
- [5] P. A. Lee, N. Nagaosa, and X.-G. Wen, Doping a Mott insulator: Physics of high-temperature superconductivity, *Reviews of Modern Physics* **78**, 17 (2006).
- [6] J. Knolle and R. Moessner, A Field Guide to Spin Liquids, *Annual Review of Condensed Matter Physics* **10**, 451 (2019).
- [7] G. Baskaran, Z. Zou, and P. Anderson, The resonating valence bond state and high- T_c superconductivity — A mean field theory, *Solid State Communications* **63**, 973 (1987).
- [8] X.-G. Wen, Quantum orders and symmetric spin liquids, *Physical Review B* **65**, 165113 (2002).
- [9] D. Poilblanc, N. Schuch, D. Pérez-García, and J. I. Cirac, Topological and entanglement properties of resonating valence bond wave functions, *Physical Review B* **86**, 014404 (2012).
- [10] W.-J. Hu, F. Becca, A. Parola, and S. Sorella, Direct evidence for a gapless Z_2 spin liquid by frustrating Néel antiferromagnetism, *Physical Review B* **88**, 060402 (2013).
- [11] Z. Y. Meng, T. C. Lang, S. Wessel, F. F. Assaad, and A. Muramatsu, Quantum spin liquid emerging in two-dimensional correlated Dirac fermions, *Nature* **464**, 847 (2010).
- [12] S. Yan, D. A. Huse, and S. R. White, Spin-Liquid Ground State of the $S = 1/2$ Kagome Heisenberg Antiferromagnet, *Science* **332**, 1173 (2011).
- [13] G. Semeghini, H. Levine, A. Keesling, S. Ebadi, T. T. Wang, D. Bluvstein, R. Verresen, H. Pichler, M. Kalinowski, R. Samajdar, A. Omran, S. Sachdev, A. Vishwanath, M. Greiner, V. Vuletić, and M. D. Lukin, Probing topological spin liquids on a programmable quantum simulator, *Science* **374**, 1242 (2021).
- [14] R. Yamamoto, H. Ozawa, D. C. Nak, I. Nakamura, and T. Fukuhara, Single-site-resolved imaging of ultracold atoms in a triangular optical lattice, *New Journal of Physics* **22**, 123028 (2020).
- [15] J. Yang, L. Liu, J. Mongkolkiattichai, and P. Schauss, Site-resolved imaging of ultracold fermions in a triangular-lattice quantum gas microscope, *PRX Quantum* **2**, 020344 (2021).
- [16] B.-Y. Sun, N. Goldman, M. Aidelsburger, and M. Bukov, Engineering and Probing Non-Abelian Chiral Spin Liquids Using Periodically Driven Ultracold Atoms, *PRX Quantum* **4**, 020329 (2023).
- [17] M. Lebrat, M. Xu, L. H. Kendrick, A. Kale, Y. Gang, P. Seetharaman, I. Morera, E. Khatami, E. Demler, and M. Greiner, Observation of nagaoka polarons in a fermi-hubbard quantum simulator, *Nature* **629**, 317 (2024).
- [18] M. L. Prichard, B. M. Spar, I. Morera, E. Demler, Z. Yan, and W. S. Bakr, Directly imaging spin polarons in a kinetically frustrated hubbard system, *Nature* **629**, 323 (2024).
- [19] H. Pan, F. Wu, and S. Das Sarma, Quantum phase diagram of a moiré-hubbard model, *Phys. Rev. B* **102**, 201104 (2020).
- [20] J. Zang, J. Wang, J. Cano, and A. J. Millis, Hartree-fock study of the moiré hubbard model for twisted bilayer transition metal dichalcogenides, *Phys. Rev. B* **104**, 075150 (2021).
- [21] N. Morales-Durán, N. C. Hu, P. Potasz, and A. H. MacDonald, Nonlocal interactions in moiré hubbard systems, *Phys. Rev. Lett.* **128**, 217202 (2022).
- [22] A. Kitaev, Anyons in an exactly solved model and beyond, *Annals of Physics* **321**, 2 (2006).
- [23] H.-C. Jiang, H. Yao, and L. Balents, Spin liquid ground state of the spin-1/2 square $J_1 - J_2$ Heisenberg model, *Physical Review B* **86**, 024424 (2012).
- [24] Y. Iqbal, W.-J. Hu, R. Thomale, D. Poilblanc, and F. Becca, Spin liquid nature in the Heisenberg $J_1 - J_2$ triangular antiferromagnet, *Physical Review B* **93**, 144411 (2016).
- [25] Z. Zhu and S. R. White, Spin liquid phase of the $S = 1/2$ $J_1 - J_2$ Heisenberg model on the triangular lattice, *Physical Review B* **92**, 041105 (2015).
- [26] A. Läuchli and D. Poilblanc, Spin-Charge Separation in Two-Dimensional Frustrated Quantum Magnets, *Physical Review Letters* **92**, 236404 (2004).
- [27] W. Kadow, L. Vanderstraeten, and M. Knap, Hole spectral function of a chiral spin liquid in the triangular lattice hubbard model, *Phys. Rev. B* **106**, 094417 (2022).
- [28] Single-hole spectra of kitaev spin liquids: from dynamical nagaoka ferromagnetism to spin-hole fractionalization, *npj Quantum Materials* **9**, 32 (2024).
- [29] R. B. Laughlin, Numerical evidence for electron decay in the two-dimensional t-J model, *Journal of Low Temperature Physics* **99**, 443 (1995).
- [30] P. Béran, D. Poilblanc, and R. Laughlin, Evidence for composite nature of quasiparticles in the 2D t-J model, *Nuclear Physics B* **473**, 707 (1996).
- [31] E. Tang, M. P. A. Fisher, and P. A. Lee, Low-energy behavior of spin-liquid electron spectral functions, *Physical Review B* **87**, 045119 (2013).
- [32] W. Rantner and X.-G. Wen, Electron Spectral Function and Algebraic Spin Liquid for the Normal State of Underdoped High T_c Superconductors, *Physical Review Letters* **86**, 3871 (2001).
- [33] W.-Y. Liu, S.-S. Gong, Y.-B. Li, D. Poilblanc, W.-Q. Chen, and Z.-C. Gu, Gapless quantum spin liquid and global phase diagram of the spin-1/2 $J_1 - J_2$ square antiferromagnetic Heisenberg model, *Science Bulletin* **67**, 1034 (2022).
- [34] L. Wang and A. W. Sandvik, Critical Level Crossings and Gapless Spin Liquid in the Square-Lattice Spin-1/2 $J_1 - J_2$ Heisenberg Antiferromagnet, *Physical Review Letters* **121**, 107202 (2018).
- [35] Y. Nomura and M. Imada, Dirac-Type Nodal Spin Liquid Revealed by Refined Quantum Many-Body Solver Using Neural-Network Wave Function, Correlation Ratio, and Level Spectroscopy, *Physical Review X* **11**, 031034 (2021).
- [36] F. Ferrari and F. Becca, Gapless spin liquid and valence-bond solid in the $J_1 - J_2$ Heisenberg model on the

- square lattice: Insights from singlet and triplet excitations, *Physical Review B* **102**, 014417 (2020).
- [37] T. Chalopin, P. Bojović, D. Bourgund, S. Wang, T. Franz, I. Bloch, and T. Hilker, *Optical superlattice for engineering Hubbard couplings in quantum simulation* (2024).
- [38] X.-Y. Song, A. Vishwanath, and Y.-H. Zhang, Doping the chiral spin liquid: Topological superconductor or chiral metal, *Physical Review B* **103**, 165138 (2021).
- [39] J. Brunkert and M. Punk, Slave-boson description of pseudogap metals in $t - J$ models, *Physical Review Research* **2**, 043019 (2020).
- [40] F. Ferrari and F. Becca, Spectral signatures of fractionalization in the frustrated Heisenberg model on the square lattice, *Physical Review B* **98**, 100405 (2018).
- [41] S.-L. Yu, W. Wang, Z.-Y. Dong, Z.-J. Yao, and J.-X. Li, Deconfinement of spinons in frustrated spin systems: Spectral perspective, *Physical Review B* **98**, 134410 (2018).
- [42] X.-G. Wen, *Quantum Field Theory of Many-Body Systems: From the Origin of Sound to an Origin of Light and Electrons*, repr ed., Oxford Graduate Texts (Oxford University Press, Oxford, 2010).
- [43] F. Ferrari and F. Becca, Dynamical Structure Factor of the $J_1 - J_2$ Heisenberg Model on the Triangular Lattice: Magnons, Spinons, and Gauge Fields, *Physical Review X* **9**, 031026 (2019).
- [44] C. L. Kane, P. A. Lee, and N. Read, Motion of a single hole in a quantum antiferromagnet, *Physical Review B* **39**, 6880 (1989).
- [45] S. Jiang, D. J. Scalapino, and S. R. White, Ground-state phase diagram of the $t - t' - J$ model, *Proceedings of the National Academy of Sciences* **118**, e2109978118 (2021).
- [46] G. Martinez and P. Horsch, Spin polarons in the $t - J$ model, *Physical Review B* **44**, 317 (1991).
- [47] N. G. Diamantis and E. Manousakis, Dynamics of string-like states of a hole in a quantum antiferromagnet: A diagrammatic Monte Carlo simulation, *New Journal of Physics* **23**, 123005 (2021).
- [48] K. K. Nielsen, T. Pohl, and G. M. Bruun, Nonequilibrium Hole Dynamics in Antiferromagnets: Damped Strings and Polarons, *Physical Review Letters* **129**, 246601 (2022).
- [49] R. B. Laughlin, Evidence for Quasiparticle Decay in Photoemission from Underdoped Cuprates, *Physical Review Letters* **79**, 1726 (1997).
- [50] W. F. Brinkman and T. M. Rice, Single-Particle Excitations in Magnetic Insulators, *Physical Review B* **2**, 1324 (1970).
- [51] G. Ji, M. Xu, L. H. Kendrick, C. S. Chiu, J. C. Brüggenjürgen, D. Greif, A. Bohrdt, F. Grusdt, E. Demler, M. Lebrat, and M. Greiner, Coupling a Mobile Hole to an Antiferromagnetic Spin Background: Transient Dynamics of a Magnetic Polaron, *Physical Review X* **11**, 021022 (2021).
- [52] J. H. Nyhegn, K. K. Nielsen, and G. M. Bruun, Equilibrium and nonequilibrium dynamics of a hole in a bilayer antiferromagnet, *Physical Review B* **106**, 155160 (2022).
- [53] M. G. Skou, T. G. Skov, N. B. Jørgensen, K. K. Nielsen, A. Camacho-Guardian, T. Pohl, G. M. Bruun, and J. J. Arlt, Non-equilibrium quantum dynamics and formation of the Bose polaron, *Nature Physics* **17**, 731 (2021).
- [54] K. K. Nielsen, L. A. P. Ardila, G. M. Bruun, and T. Pohl, Critical slowdown of non-equilibrium polaron dynamics, *New Journal of Physics* **21**, 043014 (2019).
- [55] A. Bohrdt, F. Grusdt, and M. Knap, Dynamical formation of a magnetic polaron in a two-dimensional quantum antiferromagnet, *New Journal of Physics* **22**, 123023 (2020).
- [56] S. Schmitt-Rink, C. M. Varma, and A. E. Ruckenstein, Spectral Function of Holes in a Quantum Antiferromagnet, *Physical Review Letters* **60**, 2793 (1988).
- [57] Z. Liu and E. Manousakis, Spectral function of a hole in the $t - J$ model, *Physical Review B* **44**, 2414 (1991).
- [58] F. Marsiglio, A. E. Ruckenstein, S. Schmitt-Rink, and C. M. Varma, Spectral function of a single hole in a two-dimensional quantum antiferromagnet, *Physical Review B* **43**, 10882 (1991).
- [59] Z. Liu and E. Manousakis, Dynamical properties of a hole in a Heisenberg antiferromagnet, *Physical Review B* **45**, 2425 (1992).
- [60] A. L. Chernyshev and P. W. Leung, Holes in the $t - J$ z model: A diagrammatic study, *Physical Review B* **60**, 1592 (1999).
- [61] K. K. Nielsen, M. A. Bastarrachea-Magnani, T. Pohl, and G. M. Bruun, Spatial structure of magnetic polarons in strongly interacting antiferromagnets, *Physical Review B* **104**, 155136 (2021).
- [62] J. H. Nyhegn, G. M. Bruun, and K. K. Nielsen, Wave function and spatial structure of polarons in an antiferromagnetic bilayer, *Physical Review B* **108**, 075141 (2023).
- [63] M. Charlebois and M. Imada, Single-Particle Spectral Function Formulated and Calculated by Variational Monte Carlo Method with Application to d -Wave Superconducting State, *Physical Review X* **10**, 041023 (2020).
- [64] A. Bohrdt, E. Demler, F. Pollmann, M. Knap, and F. Grusdt, Parton theory of angle-resolved photoemission spectroscopy spectra in antiferromagnetic mott insulators, *Phys. Rev. B* **102**, 035139 (2020).